Effect of the Dielectric Properties of Substrates on the Scattering Patterns of Gold Nanorods

Huanjun Chen,[†] Tian Ming,[†] Shouren Zhang,[‡] Zhao Jin,[†] Baocheng Yang,[‡] and Jianfang Wang[†,*]

[†]Department of Physics, The Chinese University of Hong Kong, Shatin, Hong Kong SAR and [‡]Institute of Nanostructured Functional Materials, Huanghe Science and Technology College, Zhengzhou, Henan 450006, China

ABSTRACT Understanding the electromagnetic interactions between plasmonic noble metal nanocrystals and different substrates is very important because a number of plasmon-based devices and applications, such as chemical and biological sensing, metamaterials, subwavelength waveguides, plasmon-enhanced photovoltaic cells, plasmon-enhanced spectroscopy, and photoswitches, require the attachment of metal nanocrystals onto various substrates. In this study, we focused on the effect of the dielectric properties of substrates on the far-field scattering patterns of supported Au nanorods. Seven types of substrates, including metals, semiconductors, and insulators, were examined. The far-field scattering patterns from individual Au nanorods were found to exhibit a doughnut shape when the modulus of the dielectric constant of the substrate is above ~7, while they appear as solid bright spots when the modulus is below ~7. This finding was validated by numerical electrodynamic calculations. Moreover, the doughnut-shaped scattering patterns are very sensitive to the spacing between the nanorod and substrate. For the nanorods supported on silicon wafers, when the spacing is increased above ~14 nm, the scattering patterns change from the doughnut shape to the solid bright spot. These results will be useful for the understanding of the plasmonic properties of noble metal nanocrystals supported on substrates and the development of a number of plasmon-based optical and optoelectronic devices at different size scales.

KEYWORDS: dielectric function · gold nanorod · mesostructured thin film · plasmon resonance · scattering · substrate

Noble metal nanocrystals exhibit rich optical properties that are derived from their localized surface plasmon resonances, the collective oscillations of the conduction electrons at the nanoscale. Their potential applications have been intensively cultivated in recent years, including ultrasensitive biosensors,[1,2] surface-enhanced Raman spectroscopy,[3,4] plasmon-enhanced fluorescence,[5,6] plasmon-enhanced light absorption for solar energy harvesting,[7] and building blocks for plasmonic circuits and metamaterials.[8,9] Many of these applications require the deposition of noble metal nanocrystals on various substrates for simple support or for integration with other components to produce complex multicomponent devices. For example, Ag nanoparticle arrays have been lithographically fabricated on mica substrates for biological sensing with high sensitivity.[10,11] Ag nanocrystals have been utilized for the fabrication of plasmon-enhanced solar cells on silicon and GaAs wafers.[12−14] Metallic nanoparticles have been aligned into one-dimensional chains on indium tin oxide (ITO) substrates for plasmonic subwavelength waveguiding[8,15,16] and into two-dimensionally ordered arrays on silica for the generation of coherent resonances with extremely small line widths.[17,18] Moreover, metallic nanostructures with complex geometries have been deposited on semiconductor and insulator substrates to fabricate metamaterials with fascinating optical properties, such as negative refraction, cloaking, and plasmon-induced transparency.[19−22] The introduction of substrates leads to the symmetry breaking of the dielectric environment surrounding noble metal nanocrystals. Such symmetry breaking can have a significant impact on the plasmonic properties of the supported nanocrystals compared to those of the corresponding freestanding ones embedded in homogeneous media. It is therefore of great importance to study and understand the effect of different supporting substrates on the plasmonic properties of noble metal nanocrystals for the design of various plasmon-based devices.

Prior studies have demonstrated much evidence on the modulation of the plasmonic properties of noble metal nanocrystals by supporting substrates. Under external optical excitation, the substrate is polarized and induces a nonuniform electric field across the metal nanocrystal. This nonuniform electric field can excite the multipolar plasmon modes of the nanocrystal. The electron oscillations associated with these plasmon modes interact, in turn, with the substrate-induced electric field. As a result, the substrate mediates the interactions among the different plasmon modes of the nanocrystal and gives

* Address correspondence to jfwang@phy.cuhk.edu.hk.

Received for review March 12, 2011 and accepted April 27, 2011.

Published online April 27, 2011
10.1021/nn200951c

rise to their hybridization.[23−26] Such a mechanism can lead to distinct alterations of the plasmon resonances of noble metal nanocrystals, such as large plasmon shifts[25,27−30] and the appearance of new plasmon modes.[25,28−31] These plasmonic alterations are strongly dependent on the dielectric properties of substrates and the spacing between the substrate and metal nanocrystal.[23,28−30] Specifically, if the substrate is a metal that exhibits propagating plasmons, the substrate−nanocrystal interactions can induce the hybridization of the plasmon modes in both components and lead to very large shifts and broadening of the plasmon resonances.[23,24] In addition, the interactions can also result in an anticrossing behavior of the plasmon resonances.[32]

Most of these previous studies have focused on the plasmon resonance spectra and energy of metal nanocrystals supported on substrates. The scattering patterns, namely, the spatial distributions of the scattered light intensity, on the other hand, play a very important role in applications that require the out-coupling of the plasmon resonances into far-field light signals for measurements and processing. Intensive research efforts are currently being devoted to the modification and control of the emission behaviors of quantum emitters, such as fluorescent molecules and quantum dots, by using plasmonic metal nanostructures as nanoantennas.[33,34] For example, a very recent study has demonstrated that unidirectional emission from individual quantum dots can be realized by assembling them to optical Yagi-Uda antennas composed of well-aligned and positioned Au nanorods.[34] In this type of application, the antenna nature of metal nanocrystals is expected to deviate remarkably from that of free-standing ones owing to the inhomogeneous dielectric environment brought about by supporting substrates. The far-field scattering intensity distributions of the supported metal nanocrystals can be strongly altered, which will be reflected by their scattering patterns. Therefore, the effect of supporting substrates on the scattering patterns of metal nanocrystals is a very important issue, which needs to be addressed.

There have been only a few studies that deal with the scattering patterns of plasmonic metal nanocrystals supported on substrates. In the recent studies of the plasmon coupling between Au nanospheres and a supporting Au film, the horizontally oriented dipole moment of the Au nanosphere is found to be damped completely by the image dipole in the Au film when the Au nanosphere is brought closer to the Au film. The complete damping gives a doughnut-shaped far-field scattering pattern.[35−37] Careful analyses have revealed that the damping of the horizontal dipole arises from the near-field interactions between the nanosphere and film, which take effect when the nanosphere−film spacing is smaller than ~15 nm.[37] The induced image charges are strongly dependent on the dielectric properties of the substrate. The far-field scattering patterns of supported metal nanocrystals are therefore expected to be affected by substrates with different dielectric properties. Up to date, the effect of different substrates on the far-field scattering patterns of supported metal nanocrystals has rarely been explored. In addition, only the scattering patterns of spherical Au nanocrystals have been considered in the previous studies. Elongated metal nanocrystals are known to be superior to their spherical counterparts owing to the larger local electric field enhancements, synthetically tunable plasmon resonance wavelengths, absorption, and scattering cross sections.[38−41] Elongated metal nanocrystals are accordingly more advantageous for various plasmon-based applications. Studying and understanding the effect of different substrates on the scattering patterns of elongated nanocrystals is therefore very crucial and will be beneficial to the plasmon-based applications with elongated nanocrystals.

Here we report on our systematic study of the far-field scattering patterns of Au nanorods deposited on different substrates, including metals, semiconductors, and insulators. Either doughnut- or solid-spot-shaped scattering patterns from the nanorods are observed. The occurrence of the different scattering patterns is strongly dependent on the modulus of the dielectric function of the substrate. Moreover, the spacing between the nanorod and substrate is also an important factor that determines the scattering patterns of the nanorod. These results suggest that supporting substrates play an important role in the scattering patterns of metal nanocrystals. The role of substrates needs to be taken into account in the development of localized plasmon-based optical and optomechanical devices.

RESULTS AND DISCUSSION

Gold Nanorods. The Au nanorods were prepared using a seeded growth method together with anisotropic oxidation.[39,42,43] Cetyltrimethylammonium bromide (CTAB) surfactant was used as the stabilizing agent. Figure 1a shows the transmission electron microscopy (TEM) image of the nanorod sample used in our experiment. The nanorods are relatively uniform in size and shape. Their average diameter, length, and aspect ratio measured from the TEM images are 42 ± 3 nm, 89 ± 7 nm, and 2.1 ± 0.2, respectively. The extinction spectrum of an aqueous dispersion of the nanorods shows a longitudinal plasmon resonance wavelength (LPRW) of 648 nm (Figure 1b). After the nanorods were washed twice by centrifugation to remove the excess stabilizing agent, they were deposited on different substrates by immersing the substrates in the nanorod solution for 30 s and then blowing them dry with nitrogen. The employed substrates include a Pt film deposited on a glass slide, a Au film deposited on a glass slide, a silicon wafer, a glass slide, an ITO film, a

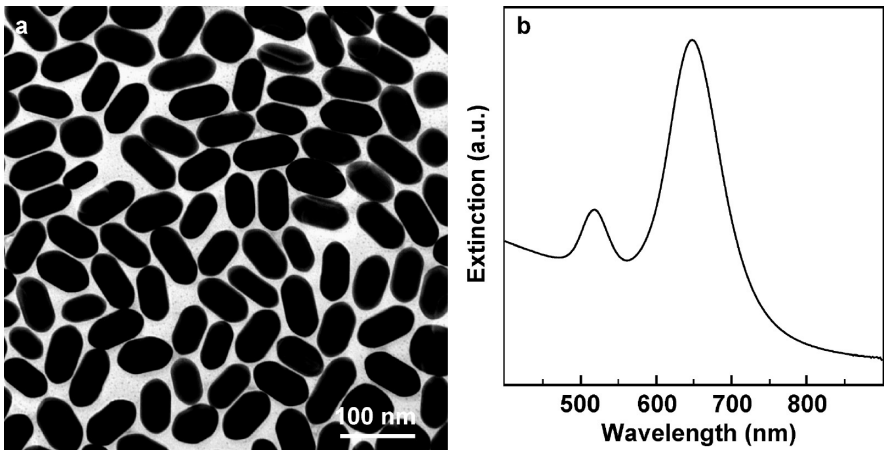

Figure 1. (a) TEM image of the Au nanorod sample. (b) Extinction spectrum of the Au nanorod sample in an aqueous solution.

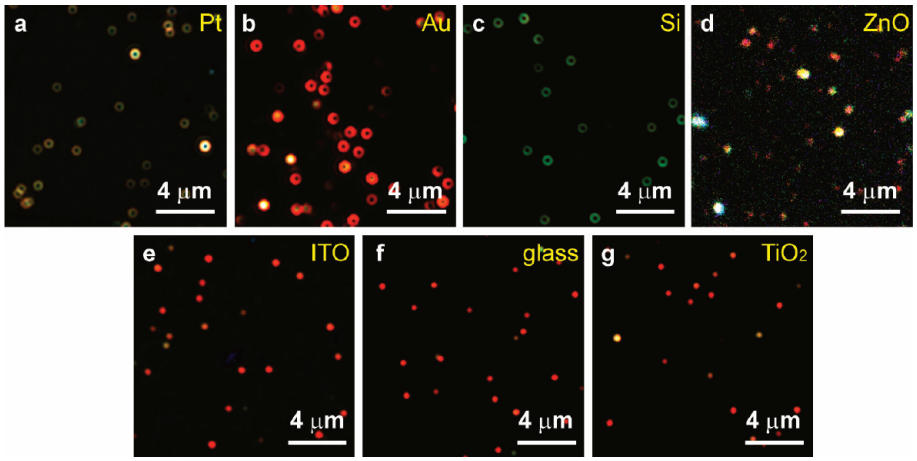

Figure 2. Far-field scattering images of the Au nanorods deposited on the different substrates: (a) Pt film, (b) Au film, (c) silicon wafer, (d) ZnO, (e) ITO film, (f) glass slide, and (g) TiO_2 film. The images were recorded with the color digital camera. The blurred scattering spots on the single-crystalline ZnO substrate arise from the smaller signal-to-noise ratio, which is caused by the considerable background scattering due to the rough surface.

single-crystalline ZnO substrate, and a mesostructured titania thin film. The number density of the nanorods on each substrate was estimated to be $1-3\ \mu m^{-2}$. The Au nanorods are capped with a CTAB bilayer. The thickness of the bilayer has been measured to be ~1.5 nm.[44] Because of the flexibility of CTAB molecules, the spacing between the nanorods and substrates is estimated to be less than 1.5 nm.

Scattering Patterns. *Experimental Observations.* The substrates carrying the Au nanorods were placed under a home-built dark-field scattering microscope for taking the scattering spectra and images with a grayscale charge-coupled device camera. The scattering images were also captured by the use of a color digital camera, which is responsive in the spectral range of 480−880 nm. Figure 2 shows the far-field scattering patterns of the Au nanorods on the different substrates. The scattering patterns of the nanorods lying on the Pt, Au, and silicon substrates are seen to be doughnut-shaped, while those of the nanorods supported on the ZnO, ITO, glass, and mesostructured TiO_2 substrates appear as solid bright spots. In addition, the scattering patterns also exhibit different colors. These observations indicate that substrates play an important role on both the spatial and spectral distributions of the light scattered from the nanorods. The occurrence of the different scattering patterns and colors can be ascribed to the different image dipoles induced by the substrates. In this study, we will focus on understanding the occurrence of the different scattering patterns, as described below.

Semi-Analytical Analysis. The size of the nanorods in our experiment is much smaller than the wavelength of the incident light. The plasmon resonances of the nanorods can be treated approximately as polarizable electric point dipoles. Because the nanorods are excited by the dark-field technique, the electric field associated with the incident light can be decomposed into two components. One is parallel to the substrate and the other perpendicular to the substrate. These two field components excite the plasmon-derived electric dipoles that are oriented parallel (in-plane) and

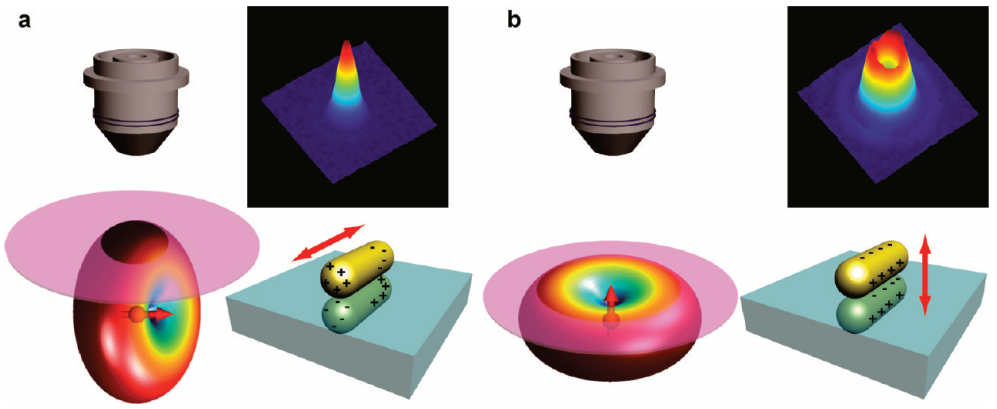

Figure 3. Schematic showing the far-field scattering patterns from the differently oriented electric dipoles. (a) Excitation field aligned parallel to the length axis of the nanorod. (b) Excitation field aligned perpendicular to the substrate. The pink plates on the radiation torus denote the regions that can be collected by the objective. The red arrows indicate the direction of the excitation polarization. The nanorod with charges is rotated relative to the dipole in the radiation torus in order to show clearly the original dipole and the image dipole in the substrate.

perpendicular (normal) to the substrate, respectively, as schematically shown in Figure 3. The excited dipoles in the nanorods induce, in turn, their respective image dipoles in the substrate. The original dipoles are coupled with their image dipoles. The coupling manner is determined by the orientation of the original dipoles relative to the substrate, and the coupling strength is dependent on the dielectric properties of the substrate and the spacing between the original dipole and the substrate. When the excitation field is aligned parallel to the length axis of the nanorod, the excited dipole and its image dipole are oriented parallel to the substrate plane (Figure 3a, lower right). The net dipole is also oriented parallel to the substrate plane. Its radiation is torus-like, with the torus plane oriented perpendicular to the substrate (Figure 3a, lower left). The vertically oriented radiation torus will be detected by the objective as a solid bright spot (Figure 3a, upper right). When the excitation field is aligned perpendicular to the substrate, the excited dipole and its image dipole are oriented perpendicular to the substrate (Figure 3b, lower right). The net dipole is also oriented perpendicular to the substrate. The torus plane of the radiation is oriented parallel to the substrate (Figure 3b, lower left). The horizontally oriented radiation torus will be detected by the objective as a doughnut-shaped pattern (Figure 3b, upper right). The detected far-field scattering pattern will be determined by the relative magnitudes of the net in-plane and normal dipoles.

The light intensity radiated from an electric dipole is characterized by a circularly symmetric, $\sin^2\theta$ spatial distribution, where θ is the angle between the dipole axis and the vector from the dipole center to the observation point. The numerical aperture of the dark-field objective used in our experiment is 0.8. This numerical aperture gives a collection angle of $\pm 53°$ relative to the optical axis of the objective. For the in-plane dipole, the light emitted within the θ range from 37 to 143° and within the azimuthal angle φ range from -53 to $+53°$ relative to the optical axis of the objective can be detected (Figure 3a, lower left). The detected far-field scattering pattern will appear as a solid bright spot. For the normal dipole, the light emitted within the θ range from 0 to 53° and within the φ range from 0 to 360° can be detected (Figure 3b, lower left). The detected far-field scattering pattern will assume a doughnut shape, which preserves the circular symmetry around the dipole axis. For the in-plane dipole, the induced image dipole in the substrate is opposite to the original one in the nanorod (Figure 3a, lower right). These two dipoles will consequently cancel each other partially and result in a reduced far-field intensity of the scattered light. On the other hand, for the normal dipole, the induced image dipole in the substrate is along the same direction as the original dipole in the nanorod (Figure 3b, lower right). The magnitude of the net dipole is increased. The total far-field intensity of the light scattered from the nanorod is a sum of the contributions from the in-plane and normal dipoles. The observed scattering pattern will depend on the relative magnitude of the net in-plane and normal dipoles. Because the magnitude of the induced image dipole is strongly dependent on the dielectric properties of the substrate, the dielectric function of the substrate is expected to play an important role in the far-field scattering pattern of the supported Au nanorods. A simple electrostatic model is employed below to reveal the relationship between them.

The interaction between the nanorod and substrate can be treated electrostatically owing to the much smaller size of the nanorod than the wavelength of the incident excitation light. In addition, because only the dipole can effectively radiate to the far field, the contributions from higher-order multipoles are neglected in the discussion of the scattering pattern. We also note that when the excitation field is aligned parallel to the substrate, both the longitudinal and transverse plasmon modes, which correspond respectively to the electron

oscillations parallel and perpendicular to the nanorod length axis, can be excited. The scattering cross section of the transverse plasmon mode of Au nanorods has been known to be generally much smaller than that of the longitudinal plasmon mode.[45] In addition, the in-plane dipole is partially reduced in magnitude by the image dipole induced in the substrate. Therefore, only the scattering from the longitudinal plasmon mode is considered when the excitation field is parallel to the substrate. The electric field arising from the original in-plane dipole, $\mathbf{E}_{//,o}$, and that from the image dipole, $\mathbf{E}_{//,i}$, at a spatial location of (x,y,z) can be expressed as[46]

$$\mathbf{E}_{//,o} = (E_x, E_y, E_z)_{//,o} = \frac{p_{//}}{4\pi\varepsilon_0\varepsilon_1}\left[\left(\frac{3x^2}{r^5} - \frac{1}{r^3}\right), \frac{3xy}{r^5}, \frac{3x(z-h)}{r^5}\right] \quad (1)$$

$$\mathbf{E}_{//,i} = (E_x, E_y, E_z)_{//,i} = \frac{p_{//}}{4\pi\varepsilon_0\varepsilon_1}\left[\left(\frac{3x^2}{r'^5} - \frac{1}{r'^3}\right), \frac{3xy}{r'^5}, \frac{3x(z+h)}{r'^5}\right] \quad (2)$$

In eqs 1 and 2, $p_{//}$ is the magnitude of the original longitudinal dipole moment, ε_0 is the vacuum permittivity, ε_1 is the dielectric constant of air, h is the spacing between the dipole and the surface of the substrate, r and r' are the radial distances measured from the centers of the original and image dipoles to the point at (x,y,z), respectively. For the used Cartesian coordinate system, the origin is set at the central point between the original and image dipoles, the x axis is along the direction of the original dipole, and the z axis is oriented perpendicular to the substrate plane and points upward. The total electric field at (x,y,z) is then

$$\mathbf{E}_{//} = \mathbf{E}_{//,o} - \frac{\varepsilon_2 - \varepsilon_1}{\varepsilon_2 + \varepsilon_1}\mathbf{E}_{//,i} \quad (3)$$

where ε_2 is the dielectric function of the substrate. For the normal and its image dipoles, the corresponding results are

$$\mathbf{E}_{\perp,o} = (E_x, E_y, E_z)_{\perp,o} = \frac{p_{\perp}}{4\pi\varepsilon_0\varepsilon_1}\left[\frac{3x(z-h)}{r^5}, \frac{3y(z-h)}{r^5}, \frac{3(z-h)^2}{r^5} - \frac{1}{r^3}\right] \quad (4)$$

$$\mathbf{E}_{\perp,i} = (E_x, E_y, E_z)_{\perp,i} = \frac{p_{\perp}}{4\pi\varepsilon_0\varepsilon_1}\left[\frac{3x(z+h)}{r'^5}, \frac{3y(z+h)}{r'^5}, \frac{3(z+h)^2}{r'^5} - \frac{1}{r'^3}\right] \quad (5)$$

$$\mathbf{E}_{\perp} = \mathbf{E}_{\perp,o} + \frac{\varepsilon_2 - \varepsilon_1}{\varepsilon_2 + \varepsilon_1}\mathbf{E}_{\perp,i} \quad (6)$$

where $p_{\perp}$ is the magnitude of the original transverse dipole moment.

In our experiment, the objective is usually positioned nearly right above the nanorod to collect the scattered light. In addition, since the most obvious difference between the doughnut-shaped and solid bright scattering patterns is the intensity at the center, we can consider only the regions that have small x and y values. Moreover, the spacing between the nanorods and substrates in our experiments is very small. As a result, r and r' are much larger than h, x, and y. From these inequalities, we obtain that $\mathbf{E}_{//,o}$ and $\mathbf{E}_{\perp,o}$ are approximately equal to $\mathbf{E}_{//,i}$ and $\mathbf{E}_{\perp,i}$, respectively. The total electric fields can then be simplified as

$$\mathbf{E}_{//} \approx \mathbf{E}_{//,o} - \frac{\varepsilon_2 - \varepsilon_1}{\varepsilon_2 + \varepsilon_1}\mathbf{E}_{//,o} = \frac{2\varepsilon_1}{\varepsilon_1 + \varepsilon_2}\mathbf{E}_{//,o} \quad (7)$$

$$\mathbf{E}_{\perp} \approx \mathbf{E}_{\perp,o} + \frac{\varepsilon_2 - \varepsilon_1}{\varepsilon_2 + \varepsilon_1}\mathbf{E}_{\perp,o} = \frac{2\varepsilon_2}{\varepsilon_1 + \varepsilon_2}\mathbf{E}_{\perp,o} \quad (8)$$

We further make the approximation that $x \to 0$, $y \to 0$, and $z \to r$. This approximation is reasonable in our experiment. The electric fields then become

$$\mathbf{E}_{//} \approx -\frac{p_{//}}{4\pi\varepsilon_0\varepsilon_1}\frac{2\varepsilon_1}{\varepsilon_1 + \varepsilon_2}\frac{1}{r^3}\hat{e}_x \quad (9)$$

$$\mathbf{E}_{\perp} \approx \frac{p_{\perp}}{4\pi\varepsilon_0\varepsilon_1}\frac{4\varepsilon_2}{\varepsilon_1 + \varepsilon_2}\frac{1}{r^3}\hat{e}_z \quad (10)$$

where $\hat{e}_x$ and $\hat{e}_z$ are the unit vectors along the x and z axes, respectively. The ratio of the electric field intensity between the in-plane and normal dipole radiation is obtained as

$$\delta = \frac{|\mathbf{E}_{//}|^2}{|\mathbf{E}_{\perp}|^2} = \frac{p_{//}^2}{p_{\perp}^2}\frac{\varepsilon_1^2}{4|\varepsilon_2|^2} \propto \frac{1}{4|\varepsilon_2|^2} \quad (11)$$

This ratio is directly related to the scattering patterns of the Au nanorods observed in our experiment because the far-field scattering intensity is proportional to $|\mathbf{E}|^2$. The proportionality comes from the fact that the magnitudes of the in-plane and normal dipoles are fixed for a given Au nanorod under a fixed excitation condition. In order to quantitatively characterize the scattering patterns, we introduce a parameter, which is defined as the ratio of the light intensity at the center of the scattering pattern to the maximum intensity (RCM) if a cross-sectional profile is drawn across the center. Typical cross-sectional profiles are given in Figure 4. For each substrate, we determined the RCM values from the scattering patterns of more than 20 nanorods and took the average.

Figure 5a shows the dispersion of $|\varepsilon|^{-2}$ for the seven different substrates, with their dielectric functions obtained from previously reported data.[47] The dielectric constant of the mesostructured titania film is obtained from a previous study.[48] For all of the substrates, $|\varepsilon|^{-2}$ is nearly constant in the spectral range of 550 to 900 nm, within which the scattering peaks of the Au nanorods are located. We therefore utilize the average values over this

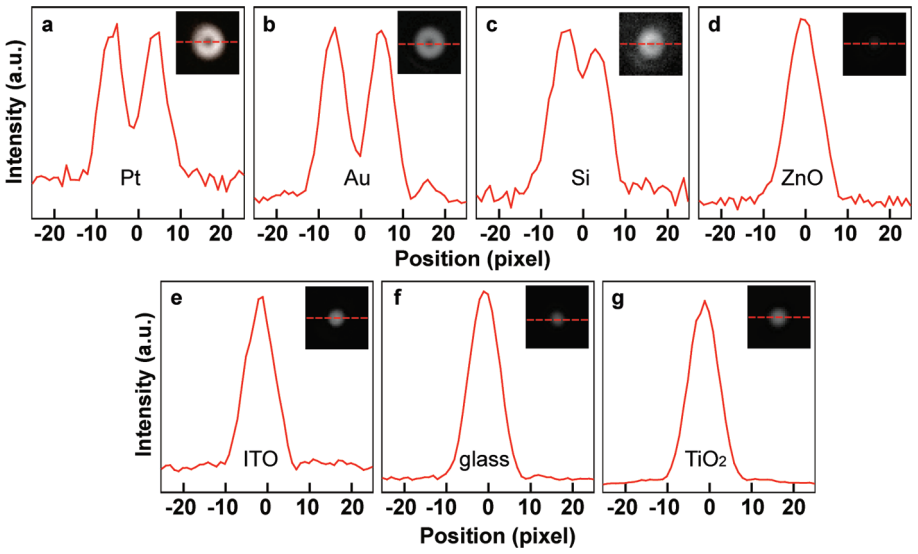

Figure 4. Typical cross-sectional profiles across the center of the scattering patterns of the Au nanorods supported on the different substrates: (a) Pt film, (b) Au film, (c) silicon wafer, (d) ZnO, (e) ITO film, (f) glass slide, and (g) TiO_2 film.

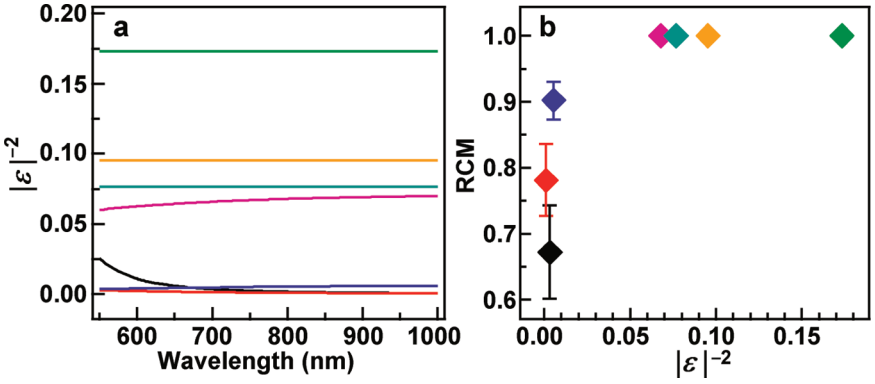

Figure 5. (a) Wavelength-dependent $|\varepsilon|^{-2}$ of the different substrates: Pt film (red), Au film (black), silicon wafer (blue), ZnO (purple), ITO film (cyan), TiO_2 film (orange), and glass slide (green). (b) Plot of the RCM value *versus* $|\varepsilon|^{-2}$.

wavelength range in the discussion below. Below the lower wavelength limit, the dielectric functions of the substrates, especially the Au film, are highly dispersive. The upper wavelength limit is determined by the detection limit of our optical system. Figure 5b shows the plot of the RCM value as a function of $|\varepsilon|^{-2}$. Except for the Pt film, the RCM value is seen to increase with $|\varepsilon|^{-2}$ and saturate at 1.0 when $|\varepsilon|^{-2}$ is larger than ~0.02. The abnormal behavior of the Pt film is believed to originate from the Cr adhesion layer used to enhance the adhesion of the Pt film to the glass slide. The dielectric property of the Pt film is altered owing to the presence of this thin Cr layer. The $|\varepsilon|^{-2}$ of the Pt film is therefore different from that of pure platinum. This result indicates that when the Au nanorod is deposited on a substrate with $|\varepsilon|^{-2}$ smaller than ~0.02 ($|\varepsilon| \sim 7$), the magnitude of the in-plane dipole will be reduced while that of the normal dipole will be enhanced by their respective image dipoles induced in the substrate. The substrate-induced changes in the magnitudes of the net in-plane and normal dipoles lead to the generation of a doughnut-shaped far-field scattering pattern. On the other hand, when the nanorod is deposited onto a substrate with $|\varepsilon|^{-2}$ larger than ~0.02, the induced image dipole for the in-plane one is not large enough to cancel the original dipole. As a result, the scattering pattern appears as a solid bright spot.

The analysis above mainly focuses on the scattering intensity at the center in order to reveal the underlying physics governing the scattering patterns of the Au nanorods supported on the different substrates. In order to describe the scattering intensity distribution, we expanded our analysis by considering the radiation of the in-plane and normal dipoles that are modified by their respective image dipoles. The quasistatic approximation was applied in our derivations. Equations 3 and 6 can be rearranged as

$$\mathbf{E}_{//} = -\nabla\left(\frac{p_{//}\cdot x}{4\pi\varepsilon_0\varepsilon_1 r^3} - \frac{\varepsilon_2-\varepsilon_1}{\varepsilon_2+\varepsilon_1}\frac{p_{//}\cdot x}{4\pi\varepsilon_0\varepsilon_1 r'^3}\right) \quad (12)$$

$$\mathbf{E}_{\perp} = -\nabla\left(\frac{p_{\perp}\cdot z}{4\pi\varepsilon_0\varepsilon_1 r^3} - \frac{\varepsilon_2+\varepsilon_1}{\varepsilon_2+\varepsilon_1}\frac{p_{\perp}\cdot z}{4\pi\varepsilon_0\varepsilon_1 r'^3}\right) \quad (13)$$

Since the measurements were carried out in the far field, r is approximately equal to r'. Equations 12 and 13 can then be written as

$$\mathbf{E}_{//} \approx -\nabla\left(\frac{2\varepsilon_1}{\varepsilon_2+\varepsilon_1}\frac{p_{//}\cdot x}{4\pi\varepsilon_0\varepsilon_1 r^3}\right) = -\nabla\left(\frac{p'_{//}\cdot x}{4\pi\varepsilon_0\varepsilon_1 r^3}\right) \quad (14)$$

$$\mathbf{E}_{\perp} \approx -\nabla\left(\frac{2\varepsilon_2}{\varepsilon_2+\varepsilon_1}\frac{p_{\perp}\cdot z}{4\pi\varepsilon_0\varepsilon_1 r^3}\right) = -\nabla\left(\frac{p'_{\perp}\cdot z}{4\pi\varepsilon_0\varepsilon_1 r^3}\right) \quad (15)$$

Equations 14 and 15 indicate that the electric field distributions in the far field under the longitudinal and perpendicular excitation can be regarded as being from two effective dipoles. These two dipoles are determined by

$$p'_{//} = \frac{2\varepsilon_1}{\varepsilon_2+\varepsilon_1}p_{//} \quad (16)$$

$$p'_{\perp} = \frac{2\varepsilon_2}{\varepsilon_2+\varepsilon_1}p_{\perp} \quad (17)$$

The far-field scattering spectrum and pattern can thereafter be calculated on the basis of eqs 16 and 17. In addition, the expressions for the magnitudes of the two dipoles clearly show that the effective dipole under the longitudinal excitation is reduced in magnitude while that under the perpendicular excitation is increased as the dielectric constant of the substrate is increased. This is qualitatively consistent with our experimental observations.

The $p_{//}$ and $p_{\perp}$ are the longitudinal and transverse plasmonic dipoles of the Au nanorod. In the quasistatic regime, they are determined by the electric polarizabilities, α_L and α_T, of the two plasmon modes. Similarly, for the effective dipoles $p'_{//}$ and $p'_{\perp}$, we can introduce two corresponding effective polarizabilities, $\alpha'_{//}$ and $\alpha'_{\perp}$. They can be obtained from

$$\alpha'_{//} = \frac{2\varepsilon_1}{\varepsilon_2+\varepsilon_1}\alpha_L \quad (18)$$

$$\alpha'_{\perp} = \frac{2\varepsilon_2}{\varepsilon_2+\varepsilon_1}\alpha_{\perp} \quad (19)$$

Au nanorods are usually treated approximately as prolate spheroids. Under this approximation, according to the Clausius–Mossotti equation,[49] α_L and α_T of the Au nanorod can be expressed as

$$\alpha_j = \frac{4\pi ab^2}{3P_j}\frac{\varepsilon_{Au}-\varepsilon_1}{\varepsilon_{Au}+\left(\frac{1-P_j}{P_j}\right)\varepsilon_1} \quad (20)$$

$$P_L = \frac{1-e^2}{e^2}\left[\frac{1}{2e}\ln\left(\frac{1+e}{1-e}\right)-1\right] \quad (21)$$

$$P_T = (1-P_L)/2 \quad (22)$$

$$e = \sqrt{1-\left(\frac{b}{a}\right)^2} \quad (23)$$

where ε_{Au} is the dielectric function of gold, j denotes L or T, standing for the longitudinal and transverse plasmon modes, respectively, P_L and P_T are the depolarization factors, a and b are the lengths of the semimajor and semimior axes, respectively. After the polarizabilities are obtained, the wavelength-dependent scattering cross sections can be determined according to

$$C_{sca,//,\perp} = \frac{1}{6\pi}\left(\frac{2\pi}{\lambda}\right)^4|\alpha'_{//,\perp}|^2 \quad (24)$$

The far-field scattering pattern, that is, the spatial distribution of the scattered light intensity, can be calculated from

$$S_{//}(\theta,z,\lambda) \propto \frac{|\alpha'_{//}|^2}{\lambda^2 z^2}\cos^4\theta \quad (25)$$

$$S_{\perp}(\theta,z,\lambda) \propto \frac{|\alpha'_{\perp}|^2}{\lambda^2 z^2}\sin^2\theta\cos^2\theta \quad (26)$$

where θ is the angle between the optical axis of the objective and the vector from the dipole center to the observation point.

On the basis of the numerical aperture of the dark-field objective used in our experiments, we calculated the far-field scattering spectra and patterns of the Au nanorod supported on the glass slide ($|\varepsilon|^{-2} = 0.1$) and silicon wafer ($|\varepsilon|^{-2} = 0.006$) according to eqs 24–26. The choice of the silicon wafer and glass slide is because the Au nanorods supported on the former give doughnut-shaped scattering patterns (Figure 2c) and the nanorods supported on the latter yield solid bright spots (Figure 2f). Figure 6 shows the obtained far-field scattering spectra and patterns. The scattering signal of the nanorod supported on the glass slide is clearly seen to be contributed dominantly by the longitudinal plasmon mode that is excited by the field oriented parallel to the nanorod length axis. The perpendicular excitation produces a much weaker scattering peak. The far-field scattering pattern is dominated by the in-plane plasmonic dipole and appears as a solid bright spot (Figure 6a–c). In contrast, when the nanorod is supported on the silicon wafer, the contribution to the scattering signal from the plasmonic dipole excited by the field oriented perpendicular to the substrate is strongly enhanced (Figure 6d–f). The far-field scattering pattern is therefore dominated by the normal plasmonic dipole and assumes a doughnut shape. The calculated scattering patterns are consistent with our experimental findings.

Electrodynamic Simulations:. We performed finite-difference time-domain (FDTD) calculations to help in

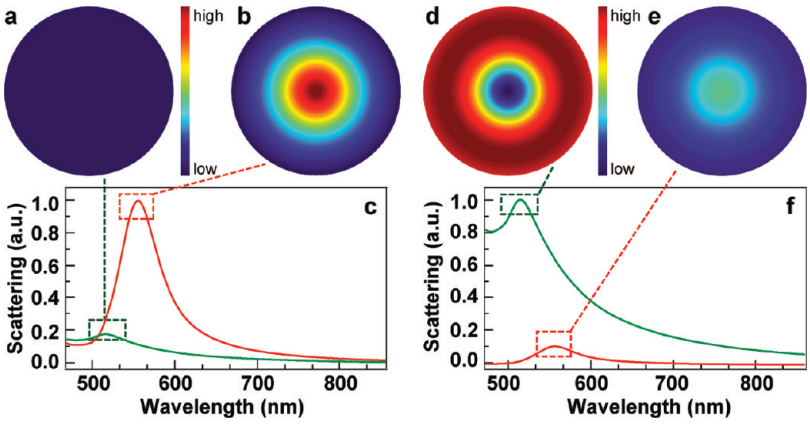

Figure 6. Far-field scattering spectra and patterns obtained from the image dipole model for the Au nanorod supported on the glass slide and silicon wafer. (a) Scattering pattern of the nanorod supported on the glass slide when the excitation field is perpendicular to the substrate. (b) Scattering pattern of the nanorod on the glass slide when the excitation field is parallel to the nanorod length axis. (c) Scattering spectra of the nanorod under the perpendicular (green) and longitudinal (red) excitation. (d−f) Corresponding scattering patterns and spectra for the nanorod supported on the silicon wafer.

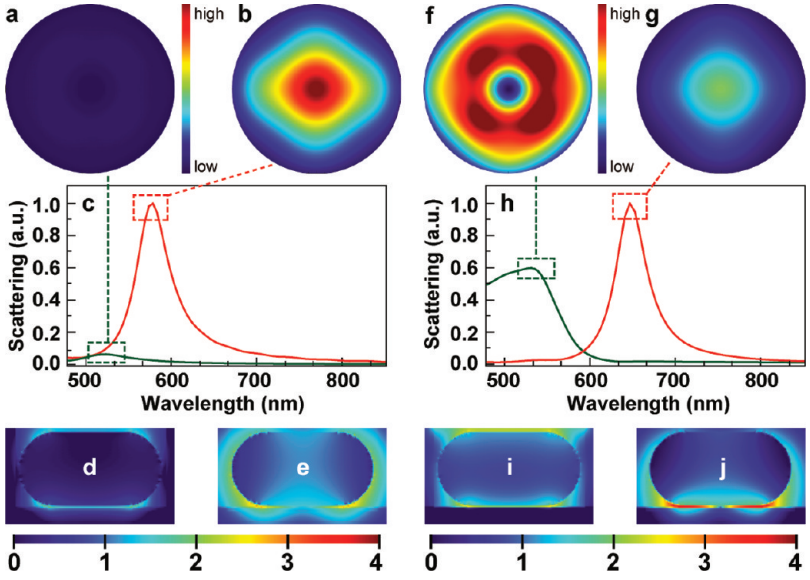

Figure 7. Field intensity enhancement contours, far-field scattering spectra, and patterns obtained from the FDTD calculations for the Au nanorods supported on the glass slide and silicon wafer. (a) Scattering pattern of the nanorod supported on the glass slide when the excitation field is perpendicular to the substrate. (b) Scattering pattern of the nanorod on the glass slide when the excitation field is parallel to the nanorod length axis. (c) Scattering spectra of the nanorod under the perpendicular (green) and longitudinal (red) excitation. (d,e) Field intensity enhancement contours of the nanorod on the glass slide under the perpendicular and longitudinal excitation, respectively. (f−j) Corresponding scattering patterns, spectra, and field intensity enhancement contours for the nanorod supported on the silicon wafer, respectively. All of the contour planes pass through the nanorod length axis and are perpendicular to the substrate. The field intensity enhancements are drawn at the logarithmic scale.

understanding the role played by the substrate on the scattering patterns of the supported nanorods. The silicon wafer and glass slide were chosen for the purpose of comparison. Figure 7 shows the calculated scattering spectra, field intensity enhancements, and corresponding far-field scattering patterns. The calculations were carried out for the excitation electric field oriented parallel to the length axis of the nanorod or perpendicular to the substrate. Similar to the results obtained from the image dipole model, the scattering signal of the nanorod on the glass slide is dominated by the longitudinal plasmon mode. The far-field scattering pattern appears as a solid bright spot (Figure 7a−c). The field intensity enhancement around the nanorod under the longitudinal excitation is also much stronger than that under the perpendicular excitation (Figure 7d, e). On the other hand, when the nanorod is supported on the silicon wafer, the normal plasmonic dipole is strongly enhanced (Figure 7f−h). In addition, the field intensity enhancement under the perpendicular excitation is also significantly strengthened (Figure 7i,j). The far-field scattering pattern therefore becomes

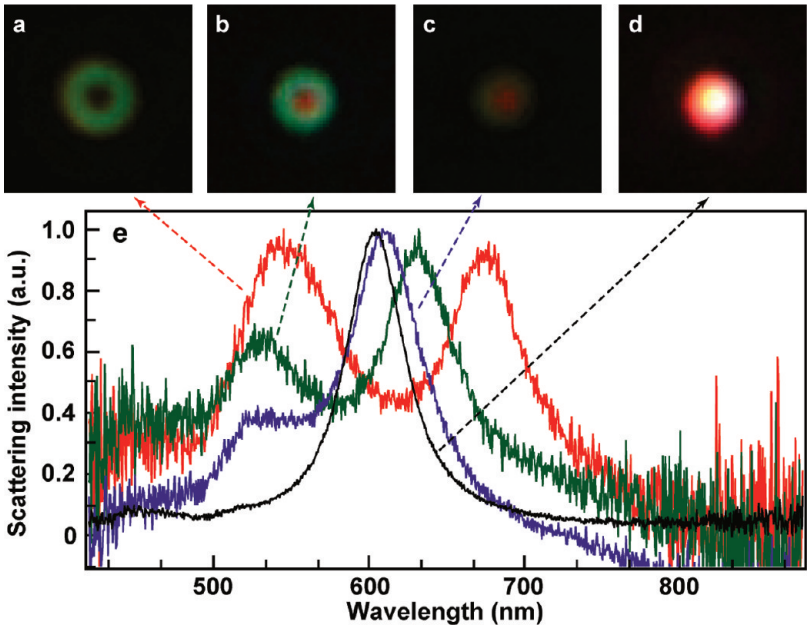

Figure 8. Far-field scattering patterns of the Au nanorods supported on the silicon wafers coated with mesostructured silica films with different thicknesses: (a) 0 nm, (b) 2.7 ± 1.2 nm, (c) 7.6 ± 0.8 nm, and (d) 13.7 ± 2.3 nm. (e) Corresponding scattering spectra.

doughnut-shaped. The results obtained from the image dipole model agree qualitatively well with those from the FDTD simulations except the relative scattering intensities between the in-plane and normal dipoles of the nanorod supported on the silicon wafer. The much stronger scattering intensity obtained from the image dipole model under the perpendicular excitation is believed to be originated from the quasistatic approximation. The size of the nanorods in our experiments is relatively large in comparison with the valid range for the quasistatic approximation, which is usually less than 30 nm.[50] The size of the nanorod can lead to phase retardation and therefore a reduction in the magnitude of the plasmonic dipole. The extent of the phase retardation depends on the direction of the excitation wave vector relative to the nanorod. In our experiments, the phase retardation under the perpendicular excitation is more severe than that under the longitudinal excitation.[51] Therefore, the scattering intensity ratio between the normal and in-plane dipoles from the image dipole model is larger than that obtained from the FDTD simulations. In addition, the scattering intensity of the calculated pattern for the normal dipole of the nanorod on the silicon wafer is larger than that for the in-plane dipole (Figure 7f,g), while the calculated scattering peak intensity for the former is smaller than that for the latter (Figure 7h). The difference can be ascribed to the use of the power monitors in the FDTD calculations. Only one power monitor is positioned above the nanorod in the calculation of the scattering patterns to simulate the collection of the scattered light by the objective. In contrast, six power monitors are set around the system, including the nanorod and substrate, in the calculation of the scattering spectra. The presence of the substrate can alter the spatial distribution of the power flux around the nanorod. Further studies are needed to fully understand this phenomenon.

Spacing Dependence. *Experimental Observations:* Equations 2 and 5 show that the electric fields of both the in-plane and normal image dipoles are functions of the spacing h between the original dipole and the substrate surface. The scattering patterns of the Au nanorods are therefore expected to be strongly dependent on the spacing between the Au nanorods and the substrate. Since silicon wafers are the most common substrates in the microelectronics and optoelectronics industries, the Au nanorod on the silicon wafer was chosen as a model system for investigating the effect of the nanorod−substrate spacing on the far-field scattering pattern. Mesostructured silica coatings were employed as the spacers between the nanorods and silicon wafers. Because the dielectric constant of the mesostructured silica coating is smaller than that of glass,[52] the presence of the coating will not alter the scattering patterns of the nanorods as discussed above. After the silicon wafers were coated with the mesostructured silica layers, which have thicknesses of 2.7 ± 1.2, 7.6 ± 0.8, and 13.7 ± 2.3 nm, respectively, the Au nanorods were deposited on the coated silicon wafers. Figure 8 shows the scattering patterns and spectra acquired from the Au nanorods supported on the coated silicon wafers. As the spacing between the nanorod and the silicon wafer is increased, the scattering pattern changes gradually from a green doughnut shape to a red solid bright spot. At the same time, the

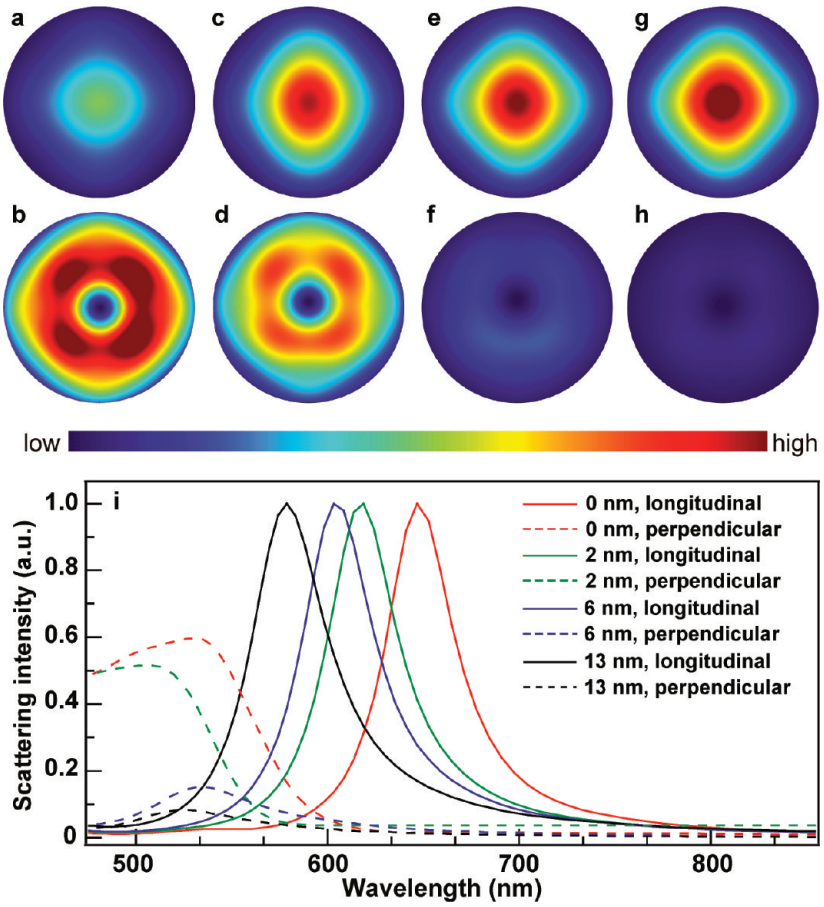

Figure 9. Spacing-dependent far-field scattering patterns and spectra obtained from the FDTD simulations for the Au nanorod supported on the silicon wafer. The thickness of the spacer layer is (a,b) 0 nm, (c,d) 2 nm, (e,f) 6 nm, and (g,h) 13 nm. The upper and lower rows show the patterns for the longitudinal and perpendicular excitation, respectively. (i) Corresponding scattering spectra.

scattering spectra also show distinct changes. When no spacer layer is present, two scattering peaks are observed. The higher-energy one arises from the normal plasmonic dipole, while the lower-energy one results from the in-plane plasmonic dipole. The former and latter are responsible for the outside green ring and central red solid spot in the scattering pattern, respectively. As the spacer layer gets thicker, the higher-energy peak becomes weaker relative to the lower-energy one. This is consistent with the idea that the outside green ring becomes weaker and the central red solid spot gets stronger. At a spacer thickness of 13.7 nm, the scattering pattern of the nanorod becomes very similar to that of the nanorod supported on the glass slide. These findings further confirm that the doughnut-shaped scattering pattern is induced through the near-field interaction between the Au nanorods and silicon wafer. The effective interaction length is found to be between 8 and 14 nm. This result needs to be taken into account in the future development of plasmonic optoelectronic devices with metal nanocrystals deposited on silicon wafers.

Electrodynamic Simulations. We further carried out the FDTD calculations of the Au nanorod supported on the silicon wafer. The spacing between the nanorod and substrate was varied by changing the thickness of the spacer layer. Figure 9 shows the scattering patterns and spectra of the nanorod under the longitudinal and perpendicular excitation. As the nanorod–substrate spacing is increased, the scattering intensity of the normal plasmonic dipole gradually fades out while that of the in-plane plasmonic dipole becomes stronger. At the same time, as the spacer layer gets thicker, the higher-energy peak becomes weaker relative to the lower-energy one. The scattering intensity ratio between the normal and in-plane dipoles is seen to decay faster than that observed experimentally. This can be ascribed to the dark-field excitation configuration used in our measurements. The oblique illumination through the dark-field objective contains a stronger light component with polarization oriented perpendicular to the substrate. This causes the normal plasmonic dipole to have a larger scattering intensity. In contrast, the normal and in-plane plasmonic dipoles are excited at equal light intensities in the FDTD calculations.

CONCLUSIONS

We have studied the effects of the dielectric properties of substrates on the far-field scattering patterns of supported Au nanorods. The excitation of the plasmon

resonances of the nanorods induces image dipoles in substrates. The image dipoles interact, in turn, with the original plasmonic dipoles in the nanorods. The interaction strongly alters the far-field scattering patterns of the nanorods. The scattering pattern of an individual Au nanorod is found to be dependent on the modulus of the dielectric function of the substrate, as well as the spacing between the nanorod and the substrate. When the nanorod is in close proximity to a substrate with a large modulus of the dielectric function, the magnitude of the in-plane dipole is reduced, while that of the normal dipole is enhanced. These changes in the magnitudes of the dipoles yield a doughnut-shaped scattering pattern. When the nanorod is supported on a substrate with a small modulus of the dielectric function, the scattering pattern is dominated by the contribution from the in-plane dipole and appear as a solid bright spot. These results can deepen our understanding of the localized surface plasmon resonances of metal nanocrystals situated in nonuniform dielectric environments. They are also of importance in the development of plasmonic optical and optoelectronic devices using noble metal nanostructures. Moreover, the dependence of the scattering patterns on the spacing between metal nanocrystals and substrates might provide an approach for the development of plasmonic sensors that can detect nanometer-scale distance changes.

EXPERIMENTAL SECTION

Growth of the Au Nanorods. The Au nanorods were prepared using a seed-mediated method together with anisotropic oxidation. Specifically, the seed solution was made by injecting a freshly prepared, ice-cold aqueous $NaBH_4$ solution (0.01 M, 0.6 mL) into an aqueous mixture composed of $HAuCl_4$ (0.01 M, 0.25 mL) and CTAB (0.1 M, 9.75 mL), which was followed by rapid inversion mixing for 2 min. The resultant seed solution was kept at room temperature for more than 2 h before use. The growth solution was made by the sequential addition of aqueous $HAuCl_4$ (0.01 M, 2 mL), $AgNO_3$ (0.01 M, 0.4 mL), HCl (1.0 M, 0.8 mL), and ascorbic acid (0.1 M, 0.32 mL) solutions into an aqueous CTAB (0.1 M, 40 mL) solution. The resultant solution was mixed by swirling for 30 s. The seed solution was first diluted by 10 times with deionized water. Then, 0.15 mL of the diluted seed solution was injected into the growth solution. The resultant reaction solution was gently mixed by inversion for 2 min and then left undisturbed overnight. The as-grown Au nanorods had an ensemble longitudinal plasmon wavelength of 740 nm. Ten milliliters of the as-grown nanorod solution was subjected to anisotropic oxidation by adding HCl (1.0 M, 0.2 mL) and H_2O_2 (30 wt %, 0.05 mL). The oxidation process was monitored by measuring the extinction spectra of the nanorod solution from time to time. When the longitudinal plasmon wavelength reached the desired value, the nanorods were washed by two cycles of centrifugation (4100*g*, 10 min) and redispersion in 0.1 M CTAB solutions to remove the excess reactants.

Preparation of the Different Substrates. The silicon wafer with a natural oxide layer ([100] oriented, Ted Pella), glass slide (Ted Pella), ITO (SPI Supplies), and single-crystalline ZnO (Wafer World) were obtained commercially. The ZnO substrate was ground with sand paper. Its surface was not as smooth as those of the other substrates. The Pt and Au substrates were fabricated, respectively, by depositing 50 nm thick Pt and 100 nm thick Au films on clean glass slides with an electron-beam evaporator (Denton Vacuum). For the Pt film, a 10 nm thick Cr layer was predeposited as an adhesion layer. The mesostructured TiO_2 film was prepared by the evaporation-induced self-assembly technique through dip coating.[53,54] The precursor solution for the titania film was prepared by first dissolving poly(ethylene oxide)−poly(propylene oxide)−poly(ethylene oxide) triblock copolymer ($EO_{20}PO_{70}EO_{20}$, P123, 0.136 g) in ethanol (1.632 g). Separately, tetraethyl orthotitanate (TEOT, 0.55 g) was added into concentrated HCl (0.42 g, ~12.1 M) and prehydrolyzed under vigorous stirring at room temperature for 5 min. The two solutions were thereafter mixed together. The molar composition was 1 TEOT/0.0097 P123/6 H_2O/1.8 HCl/14.7 ethanol. After the precursor solution was stirred at room temperature for 10 min, it was dip-coated onto a silicon wafer at a speed of 10 mm·min^{-1}. The dip-coating procedure was repeated several times to make the final thickness of the film to be ~1 μm. The consecutive layer was coated after the previous layer was dried at room temperature for 1 h. The entire film was dried in a refrigerator at 5 °C overnight. The same method was utilized to prepare the mesostructured silica films of different thicknesses on the silicon wafers as spacer layers. For the coating of the thick films (13.7 ± 2.3 nm), P123 (0.276 g) was first dissolved in ethanol (21.6 g). Tetraethyl orthosilicate (TEOS, 1.04 g) was prehydrolyzed in a solution containing dilute HCl (pH = 2, 0.54 g) and ethanol (1.2 g) by vigorous stirring at room temperature for 30 min. These two solutions were thereafter mixed together. The final molar composition of the precursor solution was 1 TEOS/0.0095 P123/6 H_2O/0.001 HCl/104.4 ethanol. The preparation of the precursor solution for the other two thin films (7.6 ± 0.8 and 2.7 ± 1.2 nm) was similar, except that the precursor solution was diluted 4 times and 16 times by ethanol, respectively. After the precursor solutions were stirred for 2 h at room temperature, they were dip-coated onto the silicon wafers at a speed of 10 mm·min^{-1}. The resultant silica films were dried at room temperature overnight before use.

Instrumentation. The extinction spectra were measured on a Hitachi U-3501 UV−visible−NIR spectrophotometer with 1 cm quartz cuvettes. Low-magnification TEM imaging was performed on an FEI CM120 microscope at 120 kV. The scattering patterns and spectra of the individual Au nanorods were recorded on a dark-field optical microscope (Olympus BX60) that was integrated with a quartz−tungsten−halogen lamp (100 W), a monochromator (Acton SpectraPro 2300i), and a charge-coupled device camera (Princeton Instruments Pixis 512B). The camera was thermoelectrically cooled to −70 °C during the measurements. A dark-field objective (100×, numerical aperture 0.80) was employed for both illuminating the nanorods with the white excitation light and collecting the scattered light. The scattered spectra from the individual nanorods were corrected by first subtracting the background spectra taken from the adjacent regions without Au nanorods and then dividing them with the calibrated response curve of the entire optical system. In addition to the grayscale scattering images recorded with the Princeton Instruments camera, color scattering images were also captured by the use of a color digital camera (Carl Zeiss, AxioCam MRC5). The thicknesses of the mesostructured SiO_2 and TiO_2 coatings were measured with an atomic force microscope (Veeco Instruments, Veeco MultiMode).

FDTD Calculations. The FDTD calculations were performed using FDTD Solutions 6.0, which was developed by Lumerical Solutions, Inc. During the calculations, an electromagnetic pulse in the wavelength range from 500 to 900 nm was launched into a box containing the target Au nanorod to simulate a propagating plane wave interacting with the nanorod. The Au nanorod and its surrounding space were divided into 0.5 nm meshes. The refractive index of the medium in the top and side regions was taken to be 1.0 and that in the bottom was set according to the

dielectric functions of the glass slide and silicon wafer. For the glass slide, the refractive index is 1.55. For the silicon wafer, the refractive index was calculated from its dielectric function.[47] The refractive index of the mesostructured silica film as the spacer layer was set as 1.35 according to previous measurements.[52] The nanorod was modeled as a cylinder capped with a hemisphere at each end. Its size was set to be the same as the average size measured from the TEM images. In order to model the light collection geometry in the experiment, a power monitor was placed right above the nanorod to record its scattering intensity in the calculations. The scattering patterns were thereafter determined.

Acknowledgment. This work was supported by CUHK block grant (Project ID: 3110061) and Hong Kong RGC Direct Allocation (Project ID: 2060417).

REFERENCES AND NOTES

1. Anker, J. N.; Hall, W. P.; Lyandres, O.; Shah, N. C.; Zhao, J.; Van Duyne, R. P. Biosensing with Plasmonic Nanosensors. *Nat. Mater.* **2008**, *7*, 442–453.
2. Sepúlveda, B.; Angelomé, P. C.; Lechuga, L. M.; Liz-Marzán, L. M. LSPR-Based Nanobiosensors. *Nano Today* **2009**, *4*, 244–251.
3. Lim, D.-K.; Jeon, K.-S.; Kim, H. M.; Nam, J.-M.; Suh, Y. D. Nanogap-Engineerable Raman-Active Nanodumbbells for Single-Molecule Detection. *Nat. Mater.* **2009**, *9*, 60–67.
4. Li, J. F.; Huang, Y. F.; Ding, Y.; Yang, Z. L.; Li, S. B.; Zhou, X. S.; Fan, F. R.; Zhang, W.; Zhou, Z. Y.; Wu, D. Y.; *et al.* Shell-Isolated Nanoparticle-Enhanced Raman Spectroscopy. *Nature* **2010**, *464*, 392–395.
5. Ming, T.; Zhao, L.; Yang, Z.; Chen, H. J.; Sun, L. D.; Wang, J. F.; Yan, C. H. Strong Polarization Dependence of Plasmon-Enhanced Fluorescence on Single Gold Nanorods. *Nano Lett.* **2009**, *9*, 3896–3903.
6. Kinkhabwala, A.; Yu, Z. F.; Fan, S. H.; Avlasevich, Y.; Müllen, K.; Moerner, W. E. Large Single-Molecule Fluorescence Enhancements Produced by a Bowtie Nanoantenna. *Nat. Photonics* **2009**, *3*, 654–657.
7. Atwater, H. A.; Polman, A. Plasmonics for Improved Photovoltaic Devices. *Nat. Mater.* **2010**, *9*, 205–213.
8. Maier, S. A.; Kik, P. G.; Atwater, H. A.; Meltzer, S.; Harel, E.; Koel, B. E.; Requicha, A. A. G. Local Detection of Electromagnetic Energy Transport below the Diffraction Limit in Metal Nanoparticle Plasmon Waveguides. *Nat. Mater.* **2003**, *2*, 229–232.
9. Ozbay, E. Plasmonics: Merging Photonics and Electronics at Nanoscale Dimensions. *Science* **2006**, *311*, 189–193.
10. Haes, A. J.; Van Duyne, R. P. A Nanoscale Optical Biosensor: Sensitivity and Selectivity of an Approach Based on the Localized Surface Plasmon Resonance Spectroscopy of Triangular Silver Nanoparticles. *J. Am. Chem. Soc.* **2002**, *124*, 10596–10604.
11. Haes, A. J.; Chang, L.; Klein, W. L.; Van Duyne, R. P. Detection of a Biomarker for Alzheimer's Disease from Synthetic and Clinical Samples Using a Nanoscale Optical Biosensor. *J. Am. Chem. Soc.* **2005**, *127*, 2264–2271.
12. Pillai, S.; Catchpole, K. R.; Trupke, T.; Green, M. A. Surface Plasmon Enhanced Silicon Solar Cells. *J. Appl. Phys.* **2007**, *101*, 093105.
13. Nakayama, K.; Tanabe, K.; Atwater, H. A. Plasmonic Nanoparticle Enhanced Light Absorption in GaAs Solar Cells. *Appl. Phys. Lett.* **2008**, *93*, 121904.
14. Beck, F. J.; Polman, A.; Catchpole, K. R. Tunable Light Trapping for Solar Cells Using Localized Surface Plasmons. *J. Appl. Phys.* **2009**, *105*, 114310.
15. Krenn, J. R.; Dereux, A.; Weeber, J. C.; Bourillot, E.; Lacroute, Y.; Goudonnet, J. P. Squeezing the Optical Near-Field Zone by Plasmon Coupling of Metallic Nanoparticles. *Phys. Rev. Lett.* **1999**, *82*, 2590–2593.
16. Maier, S. A.; Brongersma, M. L.; Kik, P. G.; Meltzer, S.; Requicha, A. A. G.; Atwater, H. A. Plasmonics—A Route to Nanoscale Optical Devices. *Adv. Mater.* **2001**, *13*, 1501–1505.
17. Kravets, V. G.; Schedin, F.; Grigorenko, A. N. Extremely Narrow Plasmon Resonances Based on Diffraction Coupling of Localized Plasmons in Arrays of Metallic Nanoparticles. *Phys. Rev. Lett.* **2008**, *101*, 087403.
18. Auguié, B.; Barnes, W. L. Collective Resonances in Gold Nanoparticle Arrays. *Phys. Rev. Lett.* **2008**, *101*, 143902.
19. Chen, H.-T.; Padilla, W. J.; Zide, J. M. O.; Gossard, A. C.; Taylor, A. J.; Averitt, R. D. Active Terahertz Metamaterial Devices. *Nature* **2006**, *444*, 597–600.
20. Valentine, J.; Zhang, S.; Zentgraf, T.; Ulin-Avila, E.; Genov, D. A.; Bartal, G.; Zhang, X. Three-Dimensional Optical Metamaterial with a Negative Refractive Index. *Nature* **2008**, *455*, 376–379.
21. Liu, N.; Guo, H. C.; Fu, L. W.; Kaiser, S.; Schwerizer, H.; Giessen, H. Three-Dimensional Photonic Metamaterials at Optical Frequencies. *Nat. Mater.* **2008**, *7*, 31–37.
22. Liu, N.; Langguth, L.; Weiss, T.; Kästel, J.; Fleischhauer, M.; Pfau, T.; Giessen, H. Plasmonic Analogue of Electromagnetically Induced Transparency at the Drude Damping Limit. *Nat. Mater.* **2009**, *8*, 758–762.
23. Nordlander, P.; Prodan, E. Plasmon Hybridization in Nanoparticles near Metallic Surfaces. *Nano Lett.* **2004**, *4*, 2209–2213.
24. Le, F.; Lwin, N. Z.; Steele, J. M.; Käll, M.; Halas, N. J.; Nordlander, P. Plasmons in the Metallic Nanoparticle-Film System as a Tunable Impurity Problem. *Nano Lett.* **2005**, *5*, 2009–2013.
25. Knight, M. W.; Wu, Y. P.; Lassiter, J. B.; Nordlander, P.; Halas, N. J. Substrates Matter: Influence of an Adjacent Dielectric on an Individual Plasmonic Nanoparticle. *Nano Lett.* **2009**, *9*, 2188–2192.
26. Wu, Y. P.; Nordlander, P. Finite-Difference Time-Domain Modeling of the Optical Properties of Nanoparticles near Dielectric Substrates. *J. Phys. Chem. C* **2010**, *114*, 7302–7307.
27. Kume, K.; Hayashi, S.; Yamamoto, K. Light Emission from Surface Plasmon Polaritons Mediated by Metallic Fine Particles. *Phys. Rev. B* **1997**, *55*, 4774–4782.
28. Okamoto, T.; Yamaguchi, I. Optical Absorption Study of the Surface Plasmon Resonance in Gold Nanoparticles Immobilized onto a Gold Substrate by Self-Assembly Technique. *J. Phys. Chem. B* **2003**, *107*, 10321–10324.
29. Lévêque, G.; Martin, O. J. F. Optical Interactions in a Plasmonic Particle Coupled to a Metallic Film. *Opt. Express* **2006**, *14*, 9971–9981.
30. Lévêque, G.; Martin, O. J. F. Tunable Composite Nanoparticle for Plasmonics. *Opt. Lett.* **2006**, *31*, 2750–2752.
31. Noguez, C. Surface Plasmons on Metal Nanoparticles: The Influence of Shape and Physical Environment. *J. Phys. Chem. C* **2007**, *111*, 3806–3819.
32. Chu, Y. Z.; Crozier, K. B. Experimental Study of the Interaction between Localized and Propagating Surface Plasmons. *Opt. Lett.* **2009**, *34*, 244–246.
33. Taminiau, T. H.; Stefani, F. D.; Segerink, F. B.; van Hulst, N. F. Optical Antennas Direct Single-Molecule Emission. *Nat. Photonics* **2008**, *2*, 234–237.
34. Curto, A. G.; Volpe, G.; Taminiau, T. H.; Kreuzer, M. P.; Quidant, R.; van Hulst, N. F. Unidirectional Emission of a Quantum Dot Coupled to a Nanoantenna. *Science* **2010**, *329*, 930–933.
35. Mock, J. J.; Hill, R. T.; Degiron, A.; Zauscher, S.; Chilkoti, A.; Smith, D. R. Distance-Dependent Plasmon Resonant Coupling between a Gold Nanoparticle and Gold Film. *Nano Lett.* **2008**, *8*, 2245–2252.
36. Chen, S.-Y.; Mock, J. J.; Hill, R. T.; Chilkoti, A.; Smith, D. R.; Lazarides, A. A. Gold Nanoparticles on Polarizable Surfaces as Raman Scattering Antennas. *ACS Nano* **2010**, *4*, 6535–6546.
37. Hill, R. T.; Mock, J. J.; Urzhumov, Y.; Sebba, D. S.; Oldenburg, S. J.; Chen, S.-Y.; Lazarides, A. A.; Chilkoti, A.; Smith, D. R. Leveraging Nanoscale Plasmonic Modes To Achieve Reproducible Enhancement of Light. *Nano Lett.* **2010**, *10*, 4150–4154.
38. Jain, P. K.; Lee, K. S.; El-Sayed, I. H.; El-Sayed, M. A. Calculated Absorption and Scattering Properties of Gold Nanoparticles of Different Size, Shape, and Composition: Applications in Biological Imaging and Biomedicine. *J. Phys. Chem. B* **2006**, *110*, 7238–7248.
39. Ni, W. H.; Kou, X. S.; Yang, Z.; Wang, J. F. Tailoring Longitudinal Surface Plasmon Wavelengths, Scattering and Absorption

Cross Sections of Gold Nanorods. *ACS Nano* **2008**, *2*, 677–686.
40. Kou, X. S.; Ni, W. H.; Tsung, C.-K.; Chan, K.; Lin, H.-Q.; Stucky, G. D.; Wang, J. F. Growth of Gold Bipyramids with Improved Yield and Their Curvature-Directed Oxidation. *Small* **2007**, *3*, 2103–2113.
41. Sönnichsen, C.; Franzl, T.; Wilk, T.; von Plessen, G.; Feldmann, J. Drastic Reduction of Plasmon Damping in Gold Nanorods. *Phys. Rev. Lett.* **2002**, *88*, 077402.
42. Ming, T.; Kou, X. S.; Chen, H. J.; Wang, T.; Tam, H.-L.; Cheah, K.-W.; Chen, J.-Y.; Wang, J. F. Ordered Gold Nanostructure Assemblies Formed by Droplet Evaporation. *Angew. Chem., Int. Ed.* **2008**, *47*, 9685–9690.
43. Tsung, C.-K.; Kou, X. S.; Shi, Q. H.; Zhang, J. P.; Yeung, M. H.; Wang, J. F.; Stucky, G. D. Selective Shortening of Single-Crystalline Gold Nanorods by Mild Oxidation. *J. Am. Chem. Soc.* **2006**, *128*, 5352–5353.
44. Zhao, F.; Du, Y.-K.; Xu, J.-K.; Liu, S.-F. Determination of Surfactant Molecular Volume by Atomic Force Microscopy. *Colloid J.* **2006**, *68*, 784–787.
45. Sun, Z. H.; Ni, W. H.; Yang, Z.; Kou, X. S.; Li, L.; Wang, J. F. pH-Controlled Reversible Assembly and Disassembly of Gold Nanorods. *Small* **2008**, *4*, 1287–1292.
46. Novotny, L.; Hecht, B. *Principles of Nano-Optics*; University Press: Cambridge, 2006; pp 358−359.
47. Palik, E. D. *Handbook of Optical Constants of Solids*; Academic Press: Boston, MA, 1985.
48. Bartl, M. H.; Boettcher, S. W.; Hu, E. L.; Stucky, G. D. Dye-Activated Hybrid Organic/Inorganic Mesostructured Titania Waveguides. *J. Am. Chem. Soc.* **2004**, *126*, 10826–10827.
49. Link, S.; El-Sayed, M. A. Spectral Properties and Relaxation Dynamics of Surface Plasmon Electronic Oscillations in Gold and Silver Nanodots and Nanorods. *J. Phys. Chem. B* **1999**, *103*, 8410–8426.
50. Slaughter, L. S.; Chang, W.-S.; Swanglap, P.; Tcherniak, A.; Khanal, B. P.; Zubarev, E. R.; Link, S. Single-Particle Spectroscopy of Gold Nanorods beyond the Quasi-Static Limit: Varying the Width at Constant Aspect Ratio. *J. Phys. Chem. C* **2010**, *114*, 4934–4938.
51. Hao, F.; Nordlander, P.; Sonnefraud, Y.; Dorpe, P. V.; Maier, S. A. Tunability of Subradiant Dipolar and Fano-Type Plasmon Resonances in Metallic Ring/Disk Cavities: Implications for Nanoscale Optical Sensing. *ACS Nano* **2009**, *3*, 643–652.
52. Yang, P. D.; Wirnsberger, G.; Huang, H. C.; Cordero, S. R.; McGehee, M. D.; Scott, B.; Deng, T.; Whitesides, G. M.; Chmelka, B. F.; Buratto, S. K.; *et al.* Mirrorless Lasing from Mesostructured Waveguides Patterned by Soft Lithography. *Science* **2000**, *287*, 465–467.
53. Alberius, P. C. A.; Frindell, K. L.; Hayward, R. C.; Kramer, E. J.; Stucky, G. D.; Chmelka, B. F. General Predictive Syntheses of Cubic, Hexagonal, and Lamellar Silica and Titania Mesostructured Thin Films. *Chem. Mater.* **2002**, *14*, 3284–3294.
54. Zhao, L.; Ming, T.; Li, G. S.; Chen, H. J.; Wang, J. F.; Yu, J. C. Monosteps on the Surfaces of Mesostructured Silica and Titania Thin Films. *Small* **2010**, *6*, 1880–1885.